J. Condensed Matter Nucl. Sci. 24 (2017) 130–145

Research Article

Increased PdD anti-Stokes Peaks are Correlated with Excess Heat Mode

Mitchell R. Swartz*
JET Energy Inc., Wellesley Hills, MA 02481, USA

Peter L. Hagelstein†
Massachusetts Institute of Technology, Cambridge, MA, USA

Abstract

Volume-enhanced Coherent Multi-wavelength Optical Reflection Electric-driven (CMORE) spectroscopy successfully differentiates active states in LANR nanomaterials. All the anti-Stokes peaks are relatively missing in the undriven mode for all of the nanostructured materials. Weak anti-Stokes peaks are elicited from Pd (and Ni and their alloy) nanostructured material in ZrO_2. But when NANOR®-type components are electrically driven, there is diversity in outcome. When driven in the avalanche mode, the anti-Stokes peaks differ considerably from those which appear during the excess heat (XSH)-producing or desired mode. The anti-Stokes peak(s) differ in energy, amount, and in what stimulates their appearance. However, normal anti-Stokes peaks return when the electrical drive creates "avalanche mode" characterized by higher electrical current at decreasing voltage. The avalanche anti-Stokes peaks are many, and they are lower energy than the XSH mode produced anti-Stokes peak (described main text). By contrast, successful cold fusion is heralded by a large increase in the anti-Stokes to Stokes (aS/S) ratio, and the generated anti-Stokes peak for the desired and XSH-producing state is very different from the avalanche-generated multiple anti-Stokes peaks. That XSH-related peak is singular and at higher energy. This distinguishing, higher energy, single, anti-Stokes peak is also not seen in the "off" state or the avalanche (undesirable) mode. Our analysis finds that the excess-heat produced anti-Stokes peak is matched to the Stokes line of PdD. We also find that the several lower energy anti-Stokes in avalanche mode (unsuccessful regarding CF/LANR) are matched to the many Stokes peaks for zirconia. In the desired electric-driven XSH-producing mode, the two-terminal deuterided NANOR®-type CF/LANR component has a measured Boltzmann Stokes ratio ∼1.3. Analysis of the phonon gain heralds $\sim 7^{\pm 0\ 15}$ acoustic phonons assisting nuclear reactions and a core peak calculated Stokes temperature of circa 1645 K. Therefore, these findings confirm a role for PdD acoustic phonons in successful CF/LANR.
 ISSN 2227-3123

Keywords: Avalanche mode, CMORE spectroscopy, Excess heat mode, NANOR®-type LANR component, Phonon gain

*Dr. Mitchell R. Swartz ScD, MD, EE, E-mail: mica@theworld.com.
†E-mail: plh@mit.edu

 ISSN 2227-3123

1. Background

1.1. Dry NANOR®-type CF/LANR preloaded components

Dry preloaded NANOR®-type LANR (lattice assisted nuclear reaction) components have been described in the literature [1–9]. NANOR®-type components have been used to investigate material science [2–9] and radiation physics [5,6] of their active LANR systems. These reports were expanded to demonstrate that several electrical transconduction states exist, but that only one is active, desired, and capable of producing excess heat (XSH) [7,8]. Later, it was demonstrated that CMORE spectroscopy [8], based on Raman spectroscopy, would be quite useful in distinguishing active LANR states because they are electrically driving them at their peak optimal operating point. This report expands that and shows (cf. Fig. 1) that for successful LANR, the anti-Stokes component matches the Stokes component for PdD. By contrast, non-active, unsuccessful, electrical avalanches have never produced XSH, and have anti-Stokes components that match the ZrO_2 Stokes components and not the PdD.

1.2. Successful LANR requires considerable engineering

LANR success is rewarded by XSH, which means that the energy producing reactions have generated *de novo* helium into the lattice ($\sim 10^{12}$ for every watt-second [10]), and there were adequate conditions to enable energy transfer to the lattice and then to appear as XSH [1,12]. There may also be other reactions.

However, the LANR method which Fleischmann and Pons first taught in March 1989 (aqueous, low impedance, $Pd/D_2O/Pt$) had problems, including inefficiency and non-reproducibility.

This created havoc for those inexperienced in metallurgy, electrochemistry, and physics [13]. One major problem to achieve successful cold fusion has been the difficulty in achieving high D/Pd loadings above $\sim$0.70 near room

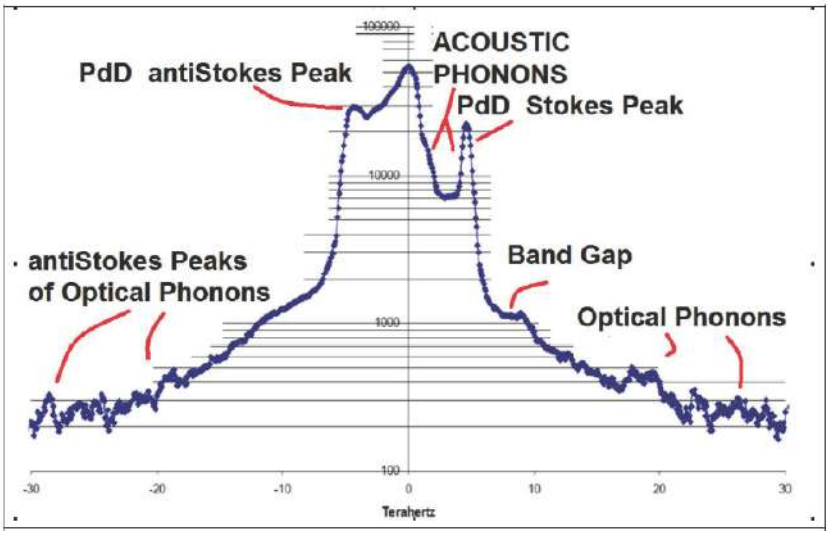

Figure 1. Log intensity Raman spectrum obtained during XSH mode (desired, non-avalanche). This is a logarithmic presentation of coherent dual wavelength electric-driven volume-enhanced reflection spectroscopy of a preloaded, correctly driven, ZrO_2PdD NANOR®-type component. The *x*-axis here presents the frequency difference from the main laser frequency. Identified are the Stokes and anti-Stokes peaks of PdD, and the band gap between acoustic and optical phonons; with the appearance of the optical phonon modes at their reported locations. The ZrO_2 Stokes peaks and anti-Stokes peaks are not labeled, but are in Fig. 6.

temperature, and then maintaining that, sometimes for weeks. Simply put, the rapid increase in deuterium chemical potential acts to limit further loading, but success requires high loading of >85% for PdD_x hydrides. In most initial efforts, loading was not even considered. Other problems have included the control of vacancies, adequate incubation time, concomitant flux, inadvertent quenching conditions, and lack of critical control of input power. Many "negative" results are due to a failure to operate the system at the optimal operating point, which is an optimum peak in the XSH and power gain curves as a function of input electrical power [13–16]. The problems with loading, and later with optimal operating point manifolds (OOPs) are why initial efforts to replicate successful LANR were so difficult and failed to show XSH [13].

1.3. Raman spectroscopy

Raman spectroscopy is a powerful tool to study vibrations within molecules, materials, and nanostructured materials to obtain knowledge of the momenta and energies from the returned optical spectrum. When used to examine materials on metal surfaces, there is a large enhancement of the electric field from the illuminating irradiation, which results in surface enhanced Raman spectroscopy (SERS). When used to examine vibrations of a lattice, the term Brillouin scattering spectroscopy is used. Raman spectroscopy was previously used to examine PdH [17–19].

2. Experimental

2.1. Materials

A NANOR®-type component is a hermetically sealed CF/LANR (cold fusion/lattice assisted nuclear reactions) nanomaterial, preloaded with D and arranged as a two-terminal electrical component. They are designed to avoid leakage, enabling stabilization and activation of these materials. The central core generating the XSH in the desired state involves ZrO_2PdNiD, ZrO_2PdD, and ZrO_2NiD and similar materials [3,20,21].

2.2. Methods

2.2.1. *Signal pickup by CMORE spectroscopy*

The black granular nanomaterials fortunately give very large signals. The volume enhancement is probably from the black nanostructured CF/LANR materials which are black, electrically insulating, and therefore will accept light deeply into the material, unlike a conductive metal electrode. A previous paper has given the experimental details of CMORE-spectroscopy [8], which uses two wavelengths of illumination from two lasers.

This was to co-illuminate the target, located below the irradiated surface, and into the volume of a sample of interest. The high intensity coherent illumination was used to elicit Rayleigh, Brillouin, and Raman bands, and then to identify the possible roles of acoustic and optical phonons during CF/LANR, and possibly distinguish the desired active, XSH-producing, state from the "off"-state, and the undesired inactive avalanche state (Fig. 2). A second lower power intensity irradiation at a second wavelength enables wavelength calibration and thus semiquantitative measurements. In this study, a 532 nm laser was used to elicit the Raman spectra, and a weaker 635 nm laser was used for calibration. The green laser (532 nm peak) had a power output level of about 150 mW. The red orange laser (635 nm peak) had a power output level of about ∼2 mW for energy calibration. Laser polarization is usually important to the degree that the nanomaterial is electrically conductive. However, LANR nanomaterials which are electrically insulating (∼megohms to gigohms or more), and are porous, black like bituminous coal, are different. There the light enters and has a volume interaction.

The sample illuminated was the core of a NANOR®-type LANR component capable of being electrically driven. Optics for collimation, control of beam direction, band pass filters, beam splitters, were used to obtain optical beam

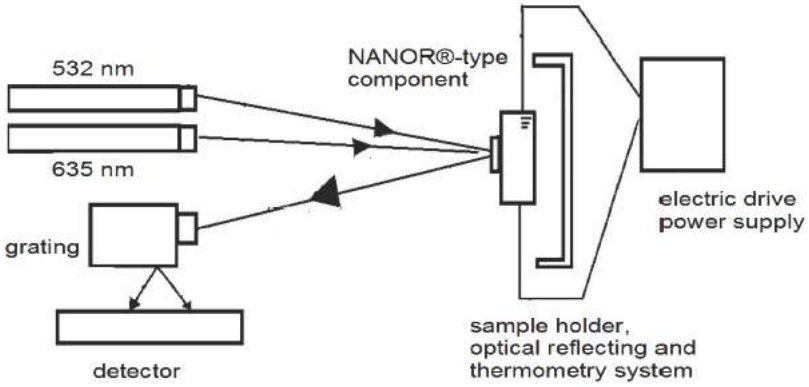

Figure 2. Schematic of coherent multi-wavelength optical reflection electric-driven spectroscopy (CMORE) experiments.

overlap on the sample's surface, facilitating interaction with the sample while being electrically driven. The important result is that illumination yields many photons which enter the black material. The multifaceted craterous surface leads to a very significant volumetric photon–sample interaction [8]. As a result of the interaction, what was initially just two initial frequencies coming from the two lasers, finally becomes a more complicated spectrum, decorated with the addition of photons of energy both above and below the two frequencies of said lasers.

2.2.2. *Determination of Stokes states*

The Boltzmann anti-Stokes to Stokes (aS/S) ratio was measured by a method enabling the simultaneous electrical driving of a ZrO_2PdD CF/LANR system in several states while simultaneously visualizing both acoustic and optical phonons using dual wavelength coherent stimulated volume-enhanced Rayleigh–Brillouin–Raman spectroscopy. When the emitted photons have less energy than the initial absorbed photon, then this energy difference is the Stokes shift. The energy goes into the lattice, and the difference is in the "red-shift" direction. On the other hand, if the emitted photon has more energy, the energy difference is called an anti-Stokes shift. That extra energy is derived from energetic phonons in a crystal lattice that give up their energy to create the "blue-shift" from the initial two frequencies. To resolve the spectra [8], the reflected (exit) beam leaves the illuminated sample through an optical slit and then passes through a diffraction grating where it is resolved into different energies (or in equivalent systems into wavelengths or frequencies). The intensity is measured by a detector such as a CCD or other sensitive photodetector. Analysis is made by integrating the incoming detected optical information which has been sorted by the grating. The final plots show the total energy of the reflected beams in a distribution of amplitude (intensity) as a function of wavelength.

2.2.3. *Determination of sample activity by calorimetry*

The LANR preloaded, stabilized NANOR®-type components are driven by a high voltage circuit up to a peak of 3000 V. This voltage is delivered in any run to either the NANOR or the ohmic control and used to thermally calibrate the calorimeter. Input power is defined as $V \times I$. There is no thermoneutral correction in denominator. Therefore, the observed power is a lower limit. The instantaneous power gain (power amplification factor (non-dimensional)) is defined as $P_{\mathrm{output}}/P_{\mathrm{input}}$. The energy is calibrated by at least one electrical joule control (ohmic resistor) used frequently, and with time integration for additional validation. The excess energy, when present, is

defined as $(P_{\mathrm{output}} - P_{\mathrm{input}}) \times$ time. Data acquisition is taken from voltage, current, and temperature sensors at multiple sites. Data acquisition sampling is at data rates of 0.20–1 Hz, with 16–24^{+} bit resolution; voltage accuracy $0.015^{\pm 0\ 005}$ V, temperature accuracy $<0.6^{\circ}$C). The noise power of the Keithley current sources driving the reactions is generally $\sim$10 nW or less [15].

2.2.4. *Electrical driving components*

The sample or component was electrically driven, or not, while it was irradiated by the two lasers while physically maintained in position. The NANOR®-type component was electrically activated and controlled, and was designed to include and use several controls: several metals and material controls such as ZrO_2Pd and ZrO_2Ni, pn-junctions (as an energy conversion control), a thermal ohmic control, a non-functional unloaded NANOR®-type component control, an inactive undriven component as a control, an inactive driven avalanche-mode component as a control, and a component driven in the desired active mode.

The electrical power supply is capable of delivering an electric current (Norton equivalent) or electric voltage (Thevenin equivalent) through the two wires which connect to the sample. The system has several electrical states, the simplest of which are "off", meaning that the sample is not electrically driven by the electrical power supply, and "on" where there may be a range of electrical driving levels of electrical power (watts). Within the holding container there are temperature detectors, and a heat flow detector, linked to a temperature measurement and analytic unit. This enables thermometry to measure any possible incremental temperature change, and therefore analysis of possible heat output from the sample.

After driving the component and the control in each run, the power and energy gain for both the component and the ohmic control were separately determined both by approximations such as input-power-normalized delta-T ($\mathrm{d}T/P_{\mathrm{in}}$), and input-power-normalized heat flow ($\mathrm{HF}/P_{\mathrm{in}}$), and also directly by semiquantitative calorimetry. In the latter, the amount of output energy is determined from the released heat produced during the temperature rise, and then comparing that to the input energy.

2.2.5. *Control – Rhodamine B deposited upon filter paper*

In order to test the system, and here to show the optical purity of the two lasers as well, dual wavelength reflection spectroscopy was performed on rhodamine B, as a control. The generated spectrum acts as a control to demonstrate the impact of the system on a rhodamine B aqueous solution of which the Stokes, anti-Stokes, and fluorescence bands are well known. Figure 3 presents the chemical structure, what a solution of the rhodamine B does to two incoming laser beams, and the resultant spectrum by this system. This control experiment used a 7.6 mmol rhodamine B solution irradiated by the two laser wavelengths (532 and 635 nm). They are labeled in the figure, and the Stokes, anti-Stokes and fluorescence bands are clearly seen, demonstrating the effectiveness of the CMORE-spectroscopic system. The second laser peak permits semiquantitative wavelength (and thus energy) calibration.

3. Results

3.1. Stokes peaks of ZrO_2

ZrO_2 has several Raman peaks between 5.7 and 19 THz. These can be seen in Fig. 4a which is a Raman spectrum of monoclinic ZrO_2 [22]. Pure zirconia's CMORE signature (ZrO_2 without any other added material) is consistent with this and is shown in Fig. 4b where the two laser initiation wavelengths of 532 and 635 nm are obvious. However, note that the first peak has an extended array of Stokes peaks observed falling to its right, in an intensity-decreasing sequence. This optical signature of pure zirconia is unusual among all the materials so far examined. ZrO_2 has a thick

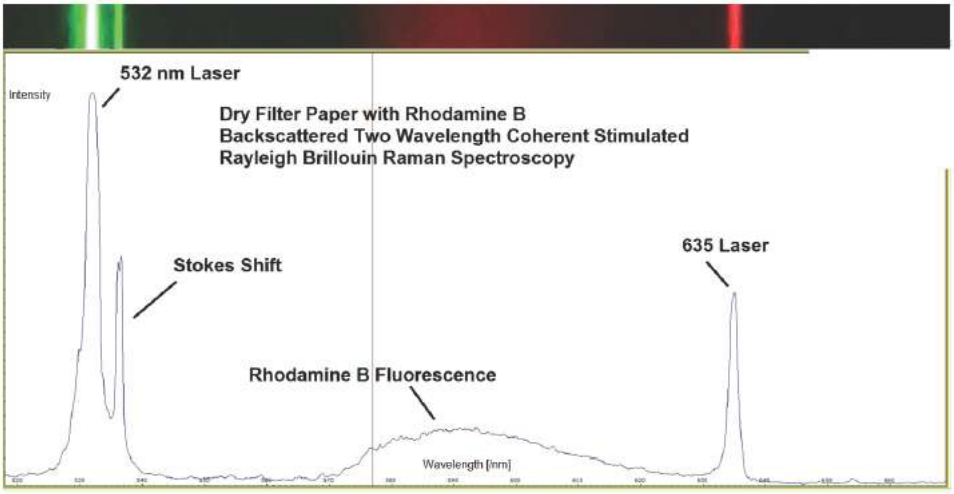

Figure 3. Spectrum from rhodamine B on filter paper. Dual wavelength reflection spectroscopy of a rhodamine B control. This CMORE-spectroscopic spectrum is a control experiment of rhodamine B (7.6 mmol aqueous solution). The vertical axis is non-linear and represents the intensity of the returned backscatter along with the reflected optical information, plotted as intensity as a function of wavelength. The horizontal axis plots the decreasing frequency to the right. The Stokes, anti-Stokes and fluorescence bands are seen in their well-known locations, and the two laser initiation wavelengths (532 and 635 nm) are seen and labeled. The actual image is located above the graph.

richness of Stokes peaks, and the anti-Stokes peaks are missing in ZrO_2 nanostructured materials observed by CMORE spectroscopy, as has been reported [8]. Given that Stokes peaks herald loss of energy of incident surface irradiation, it certainly seems possible that ZrO_2 is a molecular system able to dissipate energy through phonons (Fig. 4b). Why is there a significant loss of anti-Stokes peaks in the CF/LANR nanomaterials by this spectroscopy? Is it the same reason it is coal black?

3.2. Stokes peaks of ZrO_2 PdD – loaded and undriven (null, "off state")

Cryogenic Raman spectroscopy of PdD shows a band gap between acoustic and optical phonons, near 9 THz in those studies [23]. The PdD Phonon density of states [23] is shown in Fig. 5a. It reveals a peak before 6 THz and a band gap between 7 and 8 THz.

As a further control, the dual wavelength CMORE reflection spectroscopy was used to examine an undriven Nanor®-type component. Figure 5b is the CMORE spectrum from a loaded, electrically undriven Nanor®-type Component (ZrO_2–PdD) no driving electric current - electrically "Off". Functionally, that makes the observed optical output to be that of the raw material, ZrO_2PdD with no additional electrical drive or activation. It can be seen that the Stokes peak derived by the CMORE spectrum of ZrO_2–PdD shows the peak before 5.4 THz, consistent with the Rowe data, as are the other two peaks in the optical phonon region.

3.3. Stokes peaks of driven ZrO_2PdD in the electrical avalanche state. All CF/LANR activities are quenched by electrical avalanche breakdown

To simplify, in addition to the undriven "off" state, there are two electrically driven states for a NANOR®-type LANR component. Therefore, three (3) electrical driving states exist [7]. First, there is the undesirable "avalanche" state, associated with increasing electrical currents at falling electrical potentials. Second, by contrast, the desired "XSH"

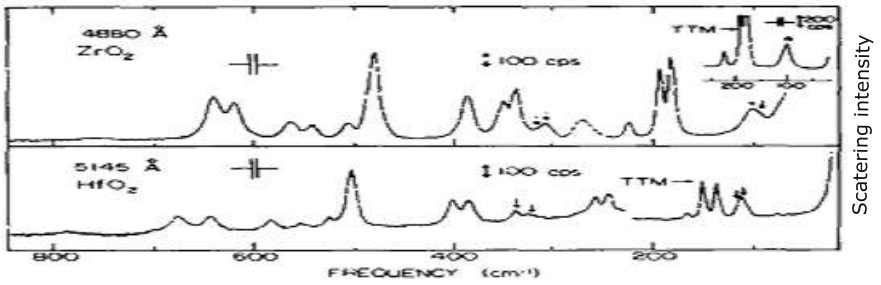

(a)

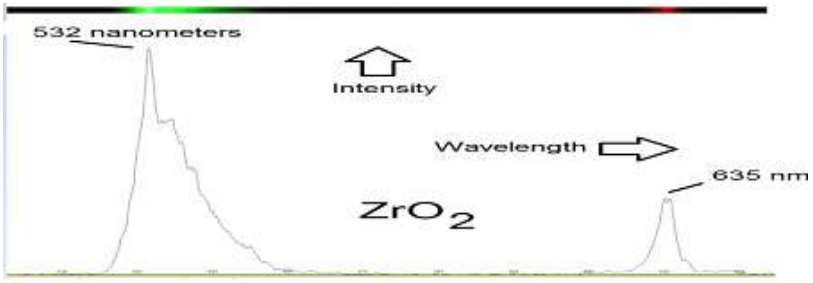

(b)

Figure 4. Raman and dual wavelength reflection CMORE spectroscopy of ZrO_2. (a) (upper) Raman spectrum from monoclinic ZrO_2 [22]. This is plotted in reverse along the x-axis compared to other figures shown. (b) (lower) CMORE-spectroscopic spectrum of ZrO_2 (zirconia without any other added material). Here, as in the rest of the figures, the horizontal axis plots the increasing wavelength to the right. The extended, and unique, multi-peak Stokes sequence of zirconia is seen along with the two laser initiation wavelengths (532 and 635 nm).

state produces very large amounts of heat beyond the normal electrical dissipation expected - XSH. In that case, high electrical impedance is maintained.

Figure 5c shows the avalanche behavior by presenting the dual wavelength electric-driven volume-enhanced reflection spectroscopic signature of a loaded (over)-driven NANOR®-type component (ZrO_2PdD) in its avalanche mode. The loaded nanomaterial, ZrO_2PdD, in a modified two terminal, dry, NANOR®-type LANR electrical component was electrically driven at 1000 V initially (direct current) which enabled a current of about 1.35 mA. Thereafter, the voltage decreased with time to about 500 V. This behavior is what is termed "avalanche mode" and usually results from excessive applied voltage. The ambient temperature was 26.7°C.

3.4. Stokes peaks of driven ZrO_2PdD in the desired XSH state

CMORE (Dual Wavelength Electric-Driven Volume-Enhanced Reflection) spectroscopy is capable of rapidly differentiating the different, and active, states in LANR nanomaterials. The functional, desired XSH state of a correctly driven NANOR®-type component (ZrO_2PdD) in its XSH mode is indicated by a unique signature using dual wavelength electric-driven volume-enhanced reflection spectroscopy. In Figs. 1, 5c and 6, the XSH mode can be seen by a unique reflected optical backscatter along with the reflected optical beams from the component in its desired XSH state.

Figure 5c shows the response of the loaded, deuterated material, ZrO_2PdD, in a NANOR®-type component to the dual wavelength reflection spectroscopy driven in all three electrical states. In this figure, the curves are superimposed.

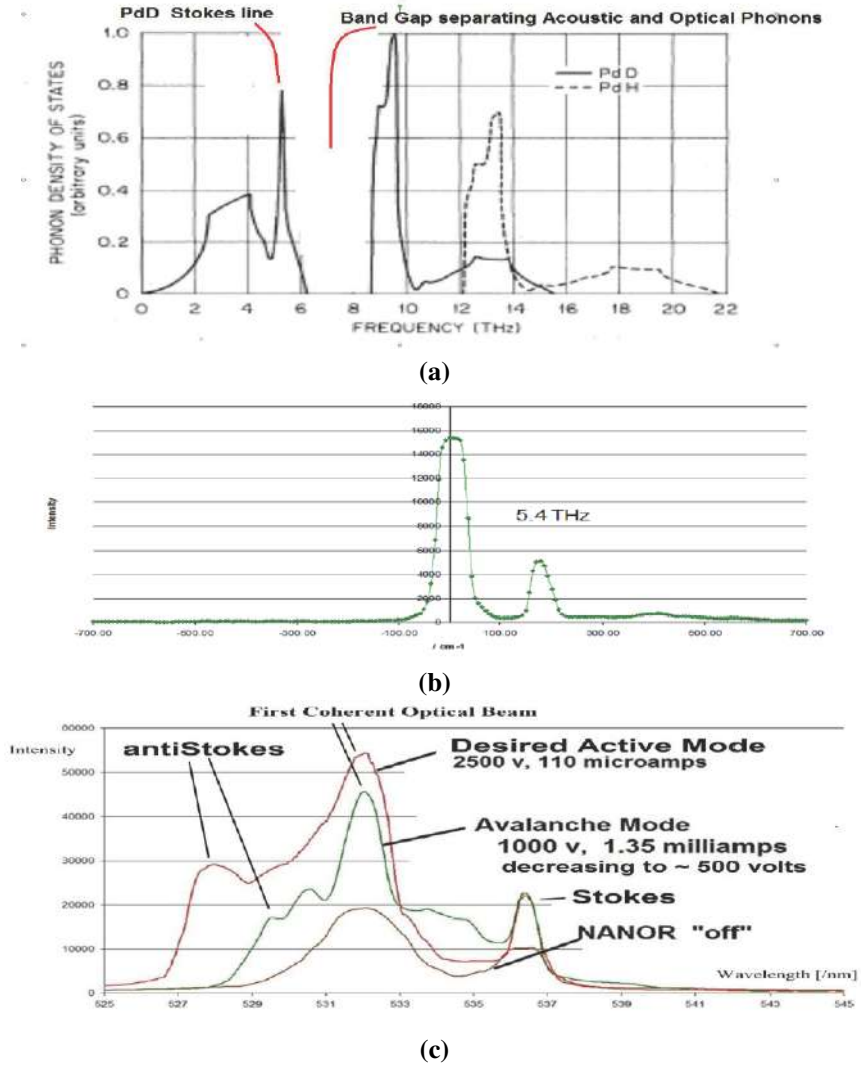

Figure 5. Comparison of PdD phonon density of states to CMORE spectra of ZrO_2–Pd and PdD. (a) (top) The PdD Phonon density of states [23] shows a peak before 6 THz and at 7–8 THz a gap. The band gap (hole) can be seen between the acoustic and optical phonons. The PdD Stokes line and band gap are marked. (b) (middle) CMORE spectrum of ZrO_2–PdD shows the peak before 5.4 THz, consistent with the Rowe data. The vertical axis represents the intensity of the returned backscatter plotted as intensity as a function of wavelength. The horizontal axis plots the decreasing frequency to the right. The output of the first laser is shown as the peak on the left side, located at 532 nm. (c) (bottom) Dual Wavelength electric-driven volume-enhanced reflection spectroscopy of a preloaded ZrO_2PdD NANOR®-type component in three electrical states (drive modes). Shown are spectra of the same NANOR®-type CF/LANR component in three different electronic states, resolved by dual wavelength coherent electric-driven volume-enhanced reflection spectroscopy. The three modes (responses) are the undriven "off"-state, the unwanted electrical avalanche mode [7], and the optimal operational state, the "Desired Active Mode" where excess energy is being released.

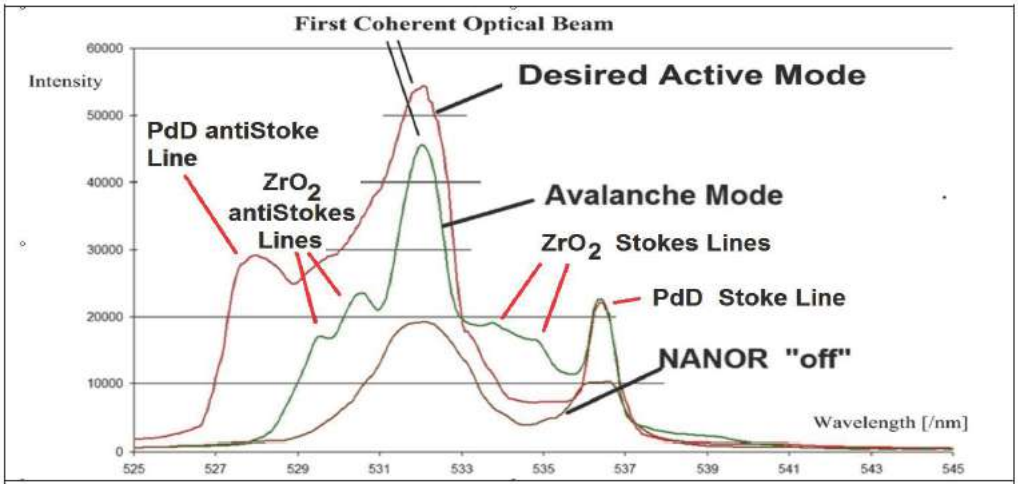

Figure 6. Assignment of anti-Stokes peaks to zirconia and PdD. These are the overlaid spectra of the three Different Electronic States Optical Signatures for the same preloaded ZrO_2PdD NANOR®-type CF/LANR component in three different electrical drive modes. Shown are spectra of the same NANOR®-type CF/LANR component (NANOR® 7-6) in three different electronic states, resolved by dual wavelength coherent electric-driven volume-enhanced reflection spectroscopy. The three modes (responses) are the undriven off-state, the unwanted electrical avalanche mode [7], and the optimal operational state, the desired active mode, where excess energy is being released. The plots show reflected optical intensity as a function of wavelength, initially from two incident coherent optical beams but then reflected by backscatter along with the initial optical beams from the core.

The nanomaterial NANOR®-type CF/LANR component was properly, correctly electrically driven at 2500 V which produced an electrical current of about 0.11 mA. The sample maintained its high impedance (compared to that seen during avalanche mode) during the very short run, and there was no electrical avalanche quenching the desired reactions. Shown is the output as intensity as a function of wavelength, as returned by backscatter along with the reflected optical beams from the volume-enhanced interactions. Note closely that in the best, most preferred, heat producing mode, the so-called "desired state", there is a much larger-than-expected anti-Stokes peak. This is the unique reflected optical output from the desired "XSH" state where large amounts of energy are being released. Intensity is shown as a function of wavelength, as returned by backscatter along with the reflected optical beams. This is the observed optical output in the desired correctly driven active "state" as observed by the diagnostic.

Figures 1, 5c, and 6 show the dramatic increase of the anti-Stokes component for an activated NANOR®-type CF/LANR component. For the activated NANOR®-type CF/LANR component, there was a major, dramatic increase of the anti-Stokes component and the aS/S ratio both greater than expected. It has been discovered that there exist increased levels of anti-Stokes-type peaks for all nanostructured materials undergoing electrical drive, however, the aS/S ratio goes above one only in active, desired mode. In fact, not only is the anti-Stokes peak of the "desired state" much higher in amplitude than expected for an initial Boltzmann statistic calculation, it is beyond any known calculated temperature, and beyond what could accrue due to curve shift to a very slight amount. These measurements demonstrate that the best XSH results occur (with the CF/LANR nanomaterial in the active, desirable mode) with an aS/S peak ratio greater than 1 (Figs. 1, 5c, and 6).

There are many critically new findings: Importantly, the unusual aS/S ratio exists ONLY with active NANOR®-type LANR component in XSH producing mode, characterized by a larger electrical impedance which precedes electrical breakdown. Thus, the CMORE spectroscopic signature heralds the "desired mode" or XSH production mode and

only results from proper drive voltage, maintaining high impedance, and avoiding quenching materials and quenching states, as discussed elsewhere [1,3,7,13,15] and demonstrated conclusively again in this report.

Furthermore, the avalanche mode-induced anti-Stokes peaks differ considerably from those observed in the XSH mode. All the anti-Stokes peaks are relatively missing in the undriven mode. But when electrically driven, there is diversity. When nanostructured NANOR®-type components are driven in avalanche mode, the anti-Stokes peaks differ considerably from those which appear during the XSH producing "desired mode". They differ in energy, and amount, and what stimulates their appearance.

The avalanche anti-Stokes peaks are many, but are lower energy than the XSH mode produced anti-Stokes peak. These match the many Stokes peaks of zirconia. By contrast, the XSH-generated anti-Stokes peak is an alternative to the avalanche-generated many peaks. That peak is singular and at one higher energy which matched the Stokes line of PdD. Thus, there appear to be two electrical heat-generating mechanisms which both dissipate energy (both applied and possibly generated internally), and they are distinguished by two entirely different end products, amounts of output heat production, and CMORE signatures.

In the unwanted mode, the anti-Stokes peaks of the electrical avalanche indicate conventional dissipation including undesirable electronic and lattice vibrations. In contrast, in the desired XSH-producing mode, the phonon gain heralded by the large anti-Stokes peaks link to unlocking the excited ^{4}He* and coupling the energy released to the lattice as whole.

3.5. ZrO_2PdD – Optical phonons

In a solid lattice, alloyed with deuterons, there are multiple modes of vibration. The acoustical phonons are those where the palladium and deuterons move in phase in the long wavelength limit, located in reciprocal space at the center of the Brillouin zone. By contrast, optical phonons have out-of-phase vibrations between neighboring atoms. They are called "optical" because in ionic crystals they can be excited by the electromagnetic radiation, with the positive ions moving one way while their negatively charged neighbors move the other way. In k (momentum)-space, the phonons appear as manifolds in two branches. The lower manifold contains the acoustical branch, and the higher manifold contains the optical branch. There is an energy gap between them when a single metal is alloyed with hydrogen or deuterium.

To better observe the optical phonons, a logarithmic vertical axis is used to enable other peaks of less intensity, like the optical phonons, to stand out. CMORE-spectroscopy resolves and measures all phonon bands, which can be seen at optical and acoustic frequencies.

In Figs. 1, 5c, and 6, the electrical driving mode of the two-terminal NANOR®-type CF/LANR component is the desired XSH mode and only results from proper drive voltage, maintaining high impedance, avoiding quenching materials and quenching states. Importantly, the phonon peaks visualized and measured in the present diagnostic, are both direct Evidence of possible optical phonons being involved, and also corroborating the indirect Evidence of Cravens, Letts, and Hagelstein [24]. The optical phonon bands are not yet well resolved in these first CMORE systems, but the need to do so clearly remains, and explorations should be fruitful.

3.6. Acoustic phonons from Pd enable XSH mode

CMORE spectroscopy has revealed a greater-than-normal intensity of anti-Stokes peaks (Figs. 1, 5c, and 6), and therefore acoustic phonon density, only during XSH mode compared to both the "off" state and compared to the avalanche mode. CF/LANR activity is now absolutely linked with acoustic phonons – and only the PdD lattice enables them. There are some other important findings.

Volume-enhanced electrically driven multiwavelength optical (CMORE) spectroscopy images acoustic and optical phonon prevalence and their diversity. Although optical phonons had previously been considered key to the energy

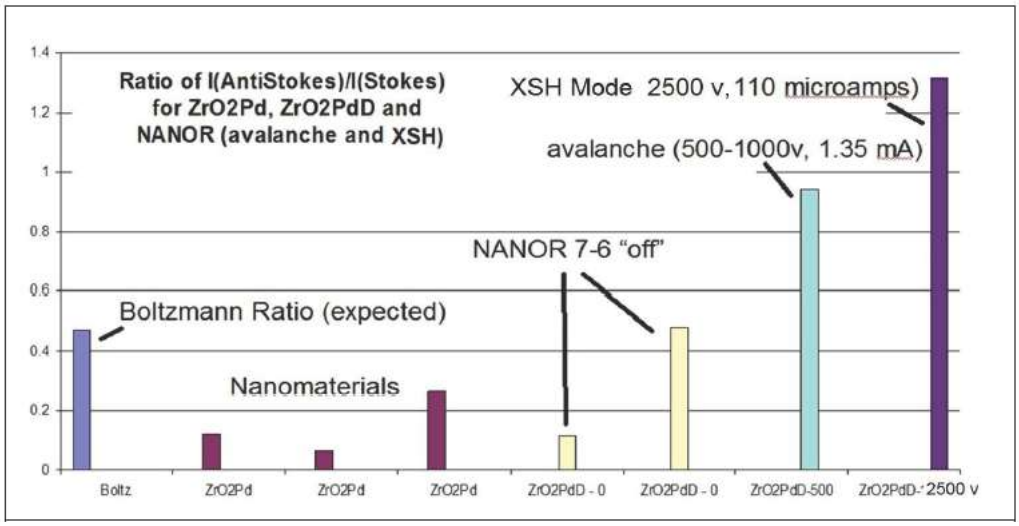

Figure 7. Results: Boltzmann ratios exceed expectations for XSH mode compared to a series of materials, and a NANOR®-type LANR component in non-XSH modes. Histogram of measured Boltzmann ratios and what is expected shown are the experimental Boltzmann ratios measured for a series of materials, and a NANOR®-type LANR component in its three modes.

transfer of ^{4}He* formed *de novo*, the present diagnostic system has determined a role for acoustic phonons in active CF/LANR systems.

The present diagnostic has revealed new direct evidence of acoustic PdD phonons in successful CF/LANR, using a NANOR®-type CF/LANR component driven correctly in its XSH mode.

Previously, cold fusion investigators have not been able to directly see phonons in their hydrogen loaded systems, although they have been inferred indirectly through beat frequency two wavelength systems [24], and thought to be mainly optical phonons [11]. Our findings confirm an important role for phonons in successful CF/LANR. They go further because this new diagnostic enables direct visualization of the actual phonon states of the hydrogen loaded material, even while it is being electrically driven. These findings confirm the role for zirconia anti-Stokes in avalanche mode (unsuccessful CF/LANR), and also herald the presence of PdD anti-Stokes peaks during successful CF/LANR. Most importantly and specifically, we have now discovered that PdD acoustic phonons result from, or are required for, successful CF/LANR.

This diagnostic has detected the existence and visualized a large single anti-Stokes peak, heralding phonon gain, which is ONLY associated with active CF/LANR XSH-production. Also, attention is directed to the fact that in the desired electric-driven XSH-producing mode, characterized by very high electrical impedance, the two-terminal deuterided NANOR®-type CF/LANR component has a measured Boltzmann–Stokes ratio $\sim$1.3.

There are several important implications. First, acoustic phonon gain either results from, or is required for, a cold fusion process which produces energy gain in its XSH mode. Successful cold fusion creates an aS/S ratio $>$1 during XSH.

Second, in retrospect, this discovery may also be consistent with the fact that only acoustic phonons are used to calculate the thermal conductivity of a material. Third, how do the XSH-generated acoustic phonons enable the creation of, or de-excitation loss of, ^{4}He* (which is the precursor to *de novo* ^{4}He seen with the XSH in aqueous systems [10,13,14])?

4. Interpretation

4.1. Summary of Boltzmann ratio results

In physics, the calculated Boltzmann statistic ratio (also known as the Boltzmann factor) is derived from the frequency and the temperature. Numerically, it is calculated from the exponential of the ratio of two energies. Those energies are the energy of the difference in energies and the thermal energy (which is the Boltzmann constant times the thermodynamic temperature in Kelvin). This is done because the ratio thus reflects the magnitude of the expected populations of the two states.

The results of measuring $R_{\mathrm{aS/S}}$ in several types of CF/LANR nanomaterials and during different types of electrical activation can be simply summarized in Fig. 7. Figure 7 is a histogram that presents both the Boltzmann statistic ratio and the Boltzmann aS/S Intensity ratios which were experimentally measured by the CMORE-spectroscopy for a series of materials, and a NANOR®-type LANR component in its three electrical modes (states). In Fig 7, the horizontal axis shows and identifies eight different categories of said ZrO_2Pd, ZrO_2PdD nanomaterial, and three electrical drive states, and what is expected normally. The vertical axis shows the amplitude of the theoretical Boltzmann statistic ratio and the experimental Boltzmann aS/S Intensity ratios.

Figure 7 shows by, histogram of the experimentally measured Boltzmann ratios, and the first column in the histogram shows exactly what is expected by calculation. To the right of that "expectation" column (expected), are shown the experimental Boltzmann ratios actually measured for a series of nanomaterials, and then a NANOR®-type LANR component in its three electrically driven modes.

Then, the next columns involve electrical activation: first electrical avalanche, and then the XSH producing (desired) mode. When values are inserted into the conventional formulae, the expected Boltzmann statistic ratio is a number between 0.4 and 0.6, as can be seen in the first column of Fig. 7. The other columns were derived experimentally for this report. The Boltzmann aS/S Intensity Ratio is derived from the actual measured relative intensities of the anti-Stokes peak divided by the intensity of the Stokes peak. Here, those values were determined by CMORE-spectroscopy. Then, the ratio is derived from the intensity of the anti-Stokes peak divided by the intensity of the Stokes peak. The histogram shows the collected information. It was obtained from the data obtained using measured Boltzmann ratios for a variety of related samples; including the relevant ZrO_2Pd nanomaterial, before heavy hydrogen is added, and after the loading deuterons to a very high level [3], and then with the two-terminal component in several electrical drive states.

4.2. Implications of the aS/S ratio >1 during XSH

Why is the anti-Stokes/Stokes ratio so high with XSH mode in ZrO_2PdD? There are important implications of an XSH-related aS/S ratio greater than one, from/during the desired cold fusion/LANR state. First, it can indicate, and so far is ONLY associated with, the desired electronic state of cold fusion (lattice assisted nuclear reaction; CF/LANR) activity in a NANOR-type CF/LANR component.

Second, that ratio is significant evidence of acoustic phonon gain, which itself is present only while the preloaded NANOR-type component is driven electrically. The highest levels indicate that the active CF/LANR system, confirmed by the CMORE-spectroscopy, is driven properly. Third, that ratio is far outside of the range expected normally by temperature alone. It passes through a region which is beyond any known calculated temperature [8]. It is a level greater than could be accounted for by a prosaic curve shift secondary to temperature.

4.3. Calculation of effective temperature during XSH

The fact that the Boltzmann Stokes ratio is $\sim$1.3 reveals more about successful cold fusion. Because the Stokes and anti Stokes energies are derivable, the effective Stokes temperature can be computed from the experimental data to

reveal the core temperature during the XSH mode. The next equation derives the calculated Boltzmann Stokes Ratio and the calculated Boltzmann Statistic ratio.

The equation involves temperature, and is

$$R_{\text{aS/S(calculated)}} = \text{Intensity(anti-Stokes)/Intensity(Stokes)} = \exp(-E_{\text{diff}}/k_{\text{B}}T), \quad (1)$$

where E_{diff} is the energy difference between the two states is 5.96×10^{-21} J and k_{B} is Boltzmann 's constant.

The calculated temperature at core is, therefore, $\sim$1645 K ($\sim$1372°C). Temperature results from the number of states available to a system and it will be important to map this finding by depth to determine its relevance as a real, physical value [8].

Table 1. Variables used in calculation

R_{s}	the Stokes ratio $=$ Intensity(anti-Stokes)/Intensity(Stokes)
k_{B}	Boltzmann's constant $= 1.38066\times10^{-23}$ J/K
T	temperature in degrees, Kelvin
E_{diff}	= ΔE an energy difference

4.4. Calculation of phonon number during XSH

How does the desired XSH mode actually create the anti-Stokes components at levels higher than observed for all other material precursor and avalanche mode? The Stokes and anti-Stokes energies are derivable, and therefore the number of phonons involved during XSH can be computed. As discussed in solid state texts [25,26], with an acoustic frequency of 4.9 $^{\pm0\ 1}$ THz, there are $\sim$7 $^{\pm0\ 15}$ phonons involved. One important point is that this is much lower than has ever been expected before in most theoretic analyses of energy transfer. Another possible point is that this number may be related to previously considerations of the palladium lattice Pd vacancy which is surrounded by six deuterons [8,27].

4.5. Spin Bose model might include acoustic phonons

Hagelstein incorporates the optical phonons in his theory. It explains the massive energy cooperative transfer from the megavoltage energy of the ^{4}He* to the lattice in a coherent de-excitation process which proceeds by way of lossy spin bosons involving phonons [11], and possibly magnons [4,9]. This study heralds that acoustic phonons have an indelible role.

4.6. Phuson theory corroborated

The proof that phonons are involved as a cohort for the XSH in active cold fusion (LANR) systems supports the PHUSON theory [12] of coherent energy transfer to the lattice. The PHUSON is the quantum of that energy transfer, in a process which is consistent with conventional physics, and where the energy then appears as XSH [1,13]. The PHUSON theory explains why there is a relative absence of strong neutron and gamma ray emissions in CF (LANR). The gamma emission branch from the excited state of ^{4}He* is actually spin-forbidden for both hot and cold fusion [12]. However, at higher hot fusion temperatures the restriction is slightly lifted. This is consistent to what is seen for both hot and cold fusion. Thus, the PHUSON theory correctly describes the relative absence of neutron emissions in CF (LANR). The only nuclear branches available are those whose band gaps are surmountable by the available activation energy (limited by the ambient temperature and incident radiation). The neutron emission branch is more than 1 MeV

above the first excited state (^{4}He*). Hot fusion has large activation energies available (it is "hot" LANR/CF is not. In LANR, given the actual much smaller amount of thermal energy, $k_{\rm B}T$, available for cold fusion ($\sim$1/25 eV), absence of adequate activation energy decisively means that that branch is NOT available, as it is for hot fusion.

4.7. Explanation for the large signals

The major problem of the Raman effect is that it produces very weak signals because the photon conversion efficiencies are less than 10^{-18}. As Sir Chandrasekhara Raman stated, the effect has "excessive feebleness" [28]. These very small signals result because the proportionality constant $\chi(3)$, known as the "third-order susceptibility", is only linearly proportional to the local oscillator density. However, that is not the case when irradiation is made using coherent lasers which yield a much larger signal because with coherent illumination there results phase-matching conditions and quadratic dependence on the number of local oscillators. Thus, even with the same selection rules, the coherent irradiation Raman effect yields a much greater signal intensity (circa 10^6 times greater) [29,30].

5. Conclusions

5.1. Implications for improvement of LANR systems

CMORE spectroscopy differentiates active states in LANR nanomaterials. The present diagnostic generates spectra in real time which are able to illuminate, visualize, and help identify at least three states for a CF/LANR material or component which is potentially active. The system can determine which state the material or component is in, in real time, even as it is electrically driven, and may be able to determine time constants for changes between levels. Most importantly, it can saliently detect the desired reactions just as products begin to appear and accumulate (e.g. heat). Therefore, it has great use because it reveals both the desired, and undesired, reactions and states and may enable better control, and possible detection of other states of operation – and therefore reactions and products.

Future studies should attempt to resolve loading of the PdD by determining the displacement of the anti-Stokes from the main peak and relating that to the Pd–Pd bond energies which decrease as loading proceeds and the lattice separation expands [31]. Other investigators may elect to use CMORE spectroscopy to resolve other peaks such as D–D.

Another advantage includes the immediate telegraphing of the state, rather than having impatient skeptics await the appearance of XSH. The use of CMORE-spectroscopy has implications for examining substates in material science and metallurgy, cold fusion physics, and in the electrical engineering of CF/LANR systems. Other spectroscopies only identify materials, while the present diagnostic reveals the electrical state of the component while continuing the means to electrically drive, control, and monitor that component and state as desired.

Volume-enhanced CMORE spectroscopy successfully differentiates active states in LANR nanomaterials. All the anti-Stokes peaks are relatively missing in the undriven mode for all of the nanostructured materials. Weak anti-Stokes peaks are elicited from Pd (and Ni and their alloy) nanostructured material in ZrO_2. But when NANOR®-type components are electrically driven, there is diversity in outcome. When driven in the avalanche mode, the anti-Stokes peaks differ considerably from those which appear during the XSH-producing, or desired, mode. The anti-Stokes peak(s) differ in energy, and amount, and differ in what stimulates their appearance. Normal anti-Stokes peaks return when the electrical drive creates "avalanche mode", characterized by higher electrical current at decreasing voltage. The avalanche anti-Stokes peaks are many, and they are lower energy than the XSH mode produced anti-Stokes peak. By contrast, successful cold fusion is heralded by a large increase in the aS/S ratio, and the generated anti-Stokes peak for the desired and XSH-producing state is very different from the avalanche-generated many anti-Stokes peaks. That XSH-related peak is singular and at higher energy. This distinguishing, higher energy, single, anti-Stokes peak (which also heralds phonon gain) is also not seen in the "off" state or the avalanche (undesirable) mode. Our analysis finds

that the excess-heat produced anti-Stokes peak is matched to the Stokes line of PdD. We also find that the several lower energy anti-Stokes in avalanche mode (unsuccessful regarding CF/LANR) are matched to the many Stokes peaks for zirconia. In the desired electric-driven XSH-producing mode, the two-terminal deuterided NANOR®-type CF/LANR component has a measured Boltzmann–Stokes ratio ∼1.3.

Analysis of the phonon gain heralds $\sim 7^{\pm 0\ 15}$ acoustic phonons assisting nuclear reactions and a core peak calculated Stokes temperature of circa 1645 K. Therefore, these findings confirm a role for PdD acoustic phonons, in the loaded lattice, during successful CF/LANR which produces XSH.

Acknowledgments

The authors acknowledge and thank for their very helpful comments, editorial assistance, and support: Gayle Verner, Jeffery Tolleson, Alex Frank, Joshua Gyllinsky, Florian Metzler, Charles Entenmann, Christy Frazier, Dennis Cravens, Dennis Letts, Frank Gordon, Pamela Mosier-Boss, Lawrence Forsley, Robert Smith, Brian Ahern, Jeff Driscoll, Louis DeChiaro, for their help, ideas and suggestions. This effort was supported by JET Energy Inc. and the New Energy Foundation. NANOR® is a registered trademark of JET Energy Incorporated. NANOR®-technology and other technology described here are protected by patents pending.

References

[1] M.R. Swartz, G. Verner, J. Tolleson and P. Hagelstein, Dry, preloaded NANOR®-type CF/LANR components, *Current Sci.* **108** (4) (2015) 595.

[2] M.R. Swartz and P.I. Hagelstein, Demonstration of energy gain from a preloaded ZrO_2–PdD nanostructured CF/LANR quantum electronic device at MIT, *J. Condensed Matter Nucl. Sci.* **13** (2014) 516. www.iscmns.org/CMNS/JCMNS-Vol13.pdf.

[3] M.R. Swartz, G. Verner and J. Tolleson, Energy gain from preloaded ZrO_2–PdNi–D nanostructured CF/LANR quantum electronic components, *J. Condensed Matter Nucl. Sci.* **13** (2014) 528. www.iscmns.org/CMNS/JCMNS-Vol13.pdf.

[4] M.R. Swartz, G. Verner, J. Tolleson, L. Wright, R. Goldbaum and P.L. Hagelstein, Amplification and restoration of energy gain using fractionated magnetic fields on ZrO_2–PdD nanostructured components, *J. Condensed Matter Nucl. Sci.* **15** (2015) 66. www.iscmns.org/CMNS/JCMNS-Vol15.pdf.

[5] M.R. Swartz, Incremental high energy emission from a ZrO_2–PdD nanostructured quantum electronic component CF/LANR, *J. Condensed Matter Nucl. Sci.* **15** (2015) 92. www.iscmns.org/CMNS/JCMNS-Vol15.pdf.

[6] M.R. Swartz, G. Verner, J. Tolleson, L. Wright, R. Goldbaum and P.L. Hagelstein, Imaging of an active NANOR®-type LANR component using CR-39, *J. Condensed Matter Nucl. Sci.* **15** (2015) 81. www.iscmns.org/CMNS/JCMNS-Vol15.pdf.

[7] M.R. Swartz, P. Hagelstein and G. Verner, Impact of electrical avalanche through a ZrO_2-NiD nanostructured CF/LANR component on its incremental excess power gain, *ICCF-19*, Padua, Italy, April 16, 2015.

[8] M.R. Swartz, Optical detection of phonon gain distinguishes an active cold fusion/LANR component, *J. Condensed Matter Nucl. Sci.* **20** (2016) 29. www.iscmns.org/CMNS/JCMNS-Vol20.pdf.

[9] M.R. Swartz, Oscillating excess power gain and magnetic domains in NANOR®-type CF/LANR component, in preparation.

[10] M.H. Miles, R.A. Hollins, B.F. Bush, J.J. Lagowski and R.E. Miles, Correlation of excess power and helium production during D_2O and H_2O electrolysis using palladium cathodes, *J. Electroanal. Chem.* **346** (1993) 99–117.

[11] P.L. Hagelstein, Current status of the theory and modeling effort on fractionation, *J. Condensed Matter Nucl. Sci.* **19** (2016)98–109.

[12] M.R. Swartz, Phusons in nuclear reactions in solids, *Fusion Technol.* **31** (1997) 228–236.

[13] M.R. Swartz, Survey of the observed excess energy and emissions in lattice assisted nuclear reactions, *J. Scientific Exploration* **23** (4) (2009) 419–436.

[14] M.R. Swartz, Excess power gain using high impedance and codepositional LANR devices monitored by calorimetry, heat flow, and paired stirling engines, *Proc. ICCF14* **1** (2008) 123. ISBN: 978-0-578-06694-3, 123 (2010). www.iscmns.org/iccf14/ProcICCF14a.pdf.

[15] M.R. Swartz and G. Verner, Excess heat from low electrical conductivity heavy water spiral-wound Pd/D_2O/Pt and Pd/D_2O–$PdCl_2$/Pt devices, *Condensed Matter Nuclear Science, Proc.ICCF-10*, World Scientific, Singapore, ISBN 981-256-564-6, 29-44 (2006) 45–54.
[16] M.R. Swartz, Consistency of the biphasic nature of excess enthalpy in solid state anomalous phenomena with the quasi-1-dimensional model of isotope loading into a material, *Fusion Technol.* **31** (1997) 63–74.
[17] R. Sherman, H.K. Birnbaum, J.A. Holy and M.V. Kleinet, *Phys. Lett.* **62A** (1977) 353.
[18] M. Fleischmann, P.R. Graves, LR. Hill and J. Robinson, *Chem. Phys. Lett.* **95** (4,5) (1983) 322–324.
[19] K. Tsuchiya, Al. Watanabe, M. Ozaki and S. Sasabe, Observation of optical phonon in palladium hydrides using Raman spectroscopy, *Proc. ICCF-14*, D.J. Nagel and M.E. Melich (Eds.), pp. 338–342. ISBN: 978-0-578-06694-3, 343, (2010).
[20] Y. Arata and Y.C. Zhang, Observation of anomalous heat release and helium-4 production from highly deuterated palladium fine particles, *Jpn. J. Appl. Phys.* **38** Part 2, No. 7A (1999) L774–L776.
[21] M.R. Swartz, Deuterium production and light water excess enthalpy experiments using nickel cathodes, *J. New Energy* **1** (3) (1996) 219. www.iscmns.org/FIC/J/JNE1N3.pdf.
[22] E. Anastassakis, B. Papanicolaou and I.M. Asher, *J. Phys. Chem. Solids* **36** (1975) 667.
[23] J. M. Rowe et al., *Phys. Rev. Lett.* **33** (1974) 1297.
[24] D. Cravens, D. Letts and P.L. Hagelstein, Progress on two-laser experiments, *Proc. ICCF15* (2009). http://lenr-canr.org/acrobat/Hagelsteinprogresson.pdf).
[25] C. Kittel, *Introduction to Solid State Physics*, Wiley, New York, 1976.
[26] N.W. Ashcroft and and N.D. Mermin, *Solid State Physics*, Holt, Rinehart and Winston, NY, 1976.
[27] D. Letts, A method to calculated excess power, *Infinite Energy* **112** (2013) 63.
[28] C.V. Raman, *Scientific Papers of C.V. Raman*, S. Ramaseshan (Ed.), Vol. 1, *The Scattering of Light*, Indian Academy of Sciences, Bangalore, India, 1988.
[29] Ji-xin Cheng, E.O. Potma and X.S. Xie, Coherent anti-Stokes Raman scattering correlation spectroscopy: probing dynamical processes with chemical selectivity, *J. Phys. Chem*. A, **106** (2002) 8561–8568.
[30] L. Evans Conor and X.S. Xie, Coherent anti-Stokes Raman scattering microscopy: chemical imaging for biology and medicine, *Ann. Rev. Anal. Chem*. **1** (2008) 883–909.
[31] P.W. Atkins and J. de Paula, *Physical Chemistry, Thermodynamics, Structure, and Change*, 10th Edition, W.H. Freeman, VA, 2014. ISBN-13: 978-1429290197.